Apical length modulates dendritic excitability in L5 pyramidal neurons

Alessandro R. Galloni[1,2], Aeron Laffere[1,3] and Ede A. Rancz[1*]
[1] The Francis Crick Institute, London, UK
[2] University College London, UK
[3] Birkbeck College, University of London, UK
*Correspondence to ede.rancz@crick.ac.uk

Abstract

Thick-tufted layer 5 (ttL5) pyramidal neurons are known for their complex morphology and diverse set of active conductances which support highly nonlinear dendritic computations. This knowledge is based primarily on recordings from neurons in the rat primary visual (V1) and somatosensory cortices. Here, we compare the active properties of mouse ttL5 neurons in V1 and in the medial secondary visual cortex (V2m) using patch-clamp recordings in acute brain slices. We find that V2m neurons lack the characteristic hallmarks of dendritic Ca^{2+} plateaus that are found in V1 neurons. Neurons in V2m also have shorter apical dendrites and we find a correlation between trunk length and excitability. Compartmental biophysical modelling revealed that the length of the apical trunk is indeed a crucial factor for determining the effect of backpropagating action potentials (bAPs) on the apical compartments. In both morphologically detailed and reduced models, neurons with short apical trunk did not display BAC firing. Finally, in the reduced model we show that peak tuft voltage increased as a function of trunk length due to a Na^{+} channel-dependent sustained broadening of bAPs in the distal trunk of long neurons. In summary, we show that ttL5 neuron active properties are not universal throughout the brain and provide new insights into how dendritic excitability can be modulated by apical dendrite length.

Introduction

An open question in neuroscience is how diverse long-range signals are integrated in the neocortex to implement circuit-wide computations. The complex dendritic morphologies of neurons throughout the brain allow segregation of inputs into functionally distinct dendritic compartments. Furthermore, most neurons have a diverse selection of voltage gated ion channels distributed throughout their dendrites. These endow dendrites with active properties that substantially increase the computational power of individual neurons (London & Häusser 2005), allowing them for instance to operate as multilayer neural networks (Beniaguev et al 2019, Harnett et al 2013, Häusser & Mel 2003, Poirazi et al 2003) and potentially enabling brain-wide learning algorithms that would otherwise be intractable (Guerguiev et al 2017, Sacramento et al 2018).

The cells that have attracted the greatest interest in this respect are layer 5 (L5) pyramidal neurons. These cells are comprised of several different subtypes, based on morphology, intrinsic physiology, and projection targets (Gouwens et al 2019, Kim et al 2015, Lur et al 2016). Of these subtypes, the deeper thick-tufted layer 5 (ttL5) pyramidal neurons (also known as L5b neurons) constitute the largest group of subcortically projecting cells and have dendritic trees extending through all layers of cortex, allowing them to integrate diverse signals from across the brain. ttL5 neurons are characterized by having a thick apical dendrite ending in a highly branched apical tuft in layer 1 (Groh et al 2010, Ramaswamy & Markram 2015). They are also generally thought to be burst spiking, mainly due to the high concentration of voltage-gated Ca^{2+} channels in their apical dendrites (Amitai et al 1993, Schiller et al 1997, Yuste et al 1994), which can induce sustained depolarizations that trigger high-frequency somatic action potential (AP) bursts. This property is exemplified by their propensity for backpropagating AP activated Ca^{2+} spike firing (BAC firing) when subject to coincident stimulation at the soma and apical dendrite (Larkum et al 1999b). Dendritic Ca^{2+} plateaus can also be triggered by high-frequency trains of somatic APs, which backpropagate into the dendrites and summate to reach the necessary voltage for Ca^{2+} channel activation (Kampa & Stuart 2006, Larkum et al 1999a, Shai et al 2015). This dendritic depolarization is visible in the somatic voltage as an after-depolarization (ADP) following the somatic spike train. The frequency response is typically sharp, with the ADP visible only above a critical frequency of approximately 100 Hz.

In addition to Ca^{2+} channel expression, morphology is also likely to have an important influence on the bursting properties of ttL5 neurons. In particular the location of oblique dendrites and the electrical coupling between the soma and dendrites is thought to be crucial for determining a neuron's integrative properties (Mainen & Sejnowski 1996, Schaefer et al 2003, van Ooyen et al 2002, Vetter et al 2001). Recent experimental work has further shown that even within the class of ttL5 neurons there can be substantial variation in intrinsic properties depending on their location within primary visual cortex (V1) or on the species from which they are recorded (Beaulieu-Laroche et al 2018, Fletcher & Williams 2019).

Present understanding of ttL5 neurons has been summarized in a general model that explains their operation as a multi-stage integrator of tuft and basal input (Larkum 2013, Larkum et al 2009, Stuart & Spruston 2015). This view has been derived mainly from recordings of ttL5 neurons in V1 and primary somatosensory cortex of 4-8 week old rats. These recordings have enabled the generation of detailed conductance-based models that reproduce the experimentally recorded somatic and dendritic spike properties (Hay et al 2011). It has also been shown that even reduced models with simplified morphology are capable of capturing most of the relevant dynamics (Bahl et al 2012).

BAC firing in ttL5 neurons has been suggested to have wide-ranging implications for cortical computation. The general top-down connectivity between cortical areas tends to target superficial layers (Cauller et al 1998, Coogan & Burkhalter 1990, Felleman & Van Essen 1991, Markov et al 2014, Rockland & Pandya 1979), and BAC firing is believed to play a major role in integrating feedforward and feedback pathways in the brain to modulate sensory perception (Takahashi et al 2016). The precise mechanism of this feedback modulation is still unclear, but may involve attention-based gain control or function as the sensory precision term within a hierarchical predictive coding framework (Bar 2006, Clark 2013, Feldman & Friston 2010, Friston 2008, Larkum 2013, Noudoost et al 2010, Rauss et al 2011). Brain-wide feedback and multimodal integration are likely to be particularly relevant in higher-order cortical areas, such as the posterior parietal cortex and secondary visual areas, where there is a convergence of multisensory, motor, navigation, and decision-making signals (Freedman & Ibos 2018).

Here we systematically compared the bursting properties of ttL5 neurons in V1 and in the medial secondary visual cortex (V2m) of adult mice. We used somatic whole-cell patch-clamp recordings, in conjunction with projection-specific retrograde labelling and a ttL5-specific Cre line. We recorded both BAC firing and critical frequency responses across these populations and found that both BAC firing and critical frequency ADPs were almost entirely absent in the V2m neurons. We also observed that across all neurons ADP size was positively correlated with the length of the apical dendrite trunk. We therefore investigated the influence of apical trunk length on burstiness in compartmental biophysical models. In these models we were able to replicate the apical length-dependence of dendritic Ca^{2+} plateaus and show that this property depends critically on the presence of voltage-gated Na+ channels in the apical trunk, which cause backpropagating potentials to be larger and broader across the apical dendrite and enable Ca^{2+} channel activation.

Results

Thick-tufted L5 neurons in V2m lack BAC firing

We made whole-cell patch clamp recordings from ttL5 pyramidal neurons in V1 and V2m in acutely prepared mouse brain slices. To ensure consistency in cell type, recordings were restricted either to neurons projecting to the lateral posterior nucleus of thalamus, identified using retrograde labelling with cholera toxin subunit B (**Supplementary Figure 1.1**), or to neurons labelled in the Glt25d2-Cre mouse line (Groh et al 2010).

To reproduce the conditions required for triggering BAC firing in ttL5 neurons, we stimulated synaptic inputs near the distal tuft in layer 1 (L1) using an extracellular electrode in conjunction with somatic stimulation through the recording electrode (**Fig. 1a**). Extracellular current pulses were adjusted to evoke either a subthreshold EPSP or a single spike at the soma. A single AP was also generated in the soma by injecting a 5 ms depolarizing pulse through the recording electrode. In V1 neurons, combined stimulation (with the L1 input triggered at the end of the somatic pulse) could evoke a prolonged plateau potential resulting in a burst of 3 APs. We repeated these experiments in ttL5 pyramidal neurons located in V2m under the same recording conditions. Upon coincident somatic AP and extracellular L1 stimulation, supralinearities in V2m were rarely observed, suggesting a much-reduced propensity for BAC firing in V2m neurons.

For the purposes of these experiments, we defined as “supralinear” any cell in which three or more spikes could be evoked following combined somatic and L1 stimulation (each evoking no more than

one spike). With this definition, in V1 supralinearity was observed in 5/22 cells, while in V2m only 1/19 cells was supralinear (**Fig. 1f**).

Thick-tufted L5 neuron in V2m lack a critical frequency ADP

To further investigate the prevalence of dendritic supralinearities in ttL5 neurons across visual cortices we recorded another hallmark of dendritic Ca^{2+} plateaus, which is the somatic ADP following a high-frequency train of somatic spikes (Larkum et al 1999a, Shai et al 2015). In these experiments, we recorded the somatic membrane potential from ttL5 neurons and evoked three action potentials using 3 ms pulses of somatic current injection at frequencies ranging from 50 Hz to 200 Hz in 10 Hz increments (**Fig. 1b**). In V1 neurons, increasing the somatic AP frequency above a critical frequency typically resulted in a sudden increase in the somatic ADP (**Fig. 1b, middle**). However, when recording in V2m under the same experimental conditions, there was usually no change in ADP, even at stimulation frequencies as high as 200 Hz (**Fig. 1b, right**). To quantify this effect, we aligned the peaks of the last spike for each frequency and measured the area of the ADP difference between the 50 Hz trace and the higher frequency traces in a 20 ms window (between 4–24 ms) following the last spike (**Fig. 1b, inset**). This measure of ADP increased sharply above the critical frequency and was often largest around the value of this frequency (**Fig. 1c**). The mean critical frequency across all cells in both V1 and V2m (excluding cells that did not have a critical frequency) was 112 ± 32 Hz (SD, n = 25, **Fig. 1d**). The maximal value of the ADP measure across all frequencies for each cell is shown in **Fig. 1e**. Recordings were made with extracellular ACSF containing either 1.5 or 2 mM $CaCl_2$ (**Supplementary Figure 1.2**). As no statistically significant difference was found between these recording conditions, **Fig. 1e** contains cells pooled from both. Neurons in V2m had significantly smaller ADP area (V1 mean = 91 ± 49 mV*ms, SD, n = 38; V2m mean = 42 ± 33 mV*ms, SD, n = 52; $p = 7.29 * 10^{-7}$, two-sample Kolmogorov-Smirnov test), reflecting that most of these cells lacked a critical frequency altogether. To obtain an unbiased count of the number of cells with this supralinearity, we split all recorded neurons into two groups using k-means clustering (with k = 2) of the unlabelled maximum ADP values pooled from both V1 and V2m. N.B. that in this experiment the "supralinear" classification was defined differently than in the experiment shown in **Fig. 1a**. In both experiments, the percentage of neurons classified as "supralinear" (summarized in **Fig. 1f**) was more than three times higher in V1 than in V2m. In both the BAC firing and ADP experiments mentioned above, bursting was typically also apparent in the spiking response to a long (500 ms) depolarization at the soma. While all ttL5 neurons are generally characterized by a spike doublet at the beginning of the current step, in bursting neurons there is also a critical current step above which the initial spike burst is substantially larger, usually with 3 or 4 spikes and a deeper afterhyperpolarization (**Supplementary Figure 1.3**).

These results show a much-diminished dendritic excitability, and as such different integrative properties, in V2m ttL5 neurons compared to V1 ttL5 neurons under the same conditions and in the same operational ranges. Previous research has indicated the length of the apical trunk as a possible factor involved in determining the dendritic excitability of ttL5 neurons in V1 (Fletcher & Williams 2019). We have thus reconstructed the apical trunk of 22 V1 and 26 V2m neurons from those recorded. Apical trunk lengths were significantly shorter in V2m than in V1 (V1 mean = 400 ± 61 µm, SD; V2m mean = 322 ± 70 µm, SD; $p = 1.92*10^{-4}$, two-sample t-test, **Fig. 1g**). Additionally, there was a correlation between maximal ADP integral values and apical trunk length across the two populations ($p = 2.81*10^{-2}$; t-test). These results suggest that there may be an interaction between apical trunk length and dendritic excitability—the longer the trunk, the more excitable the neuron.

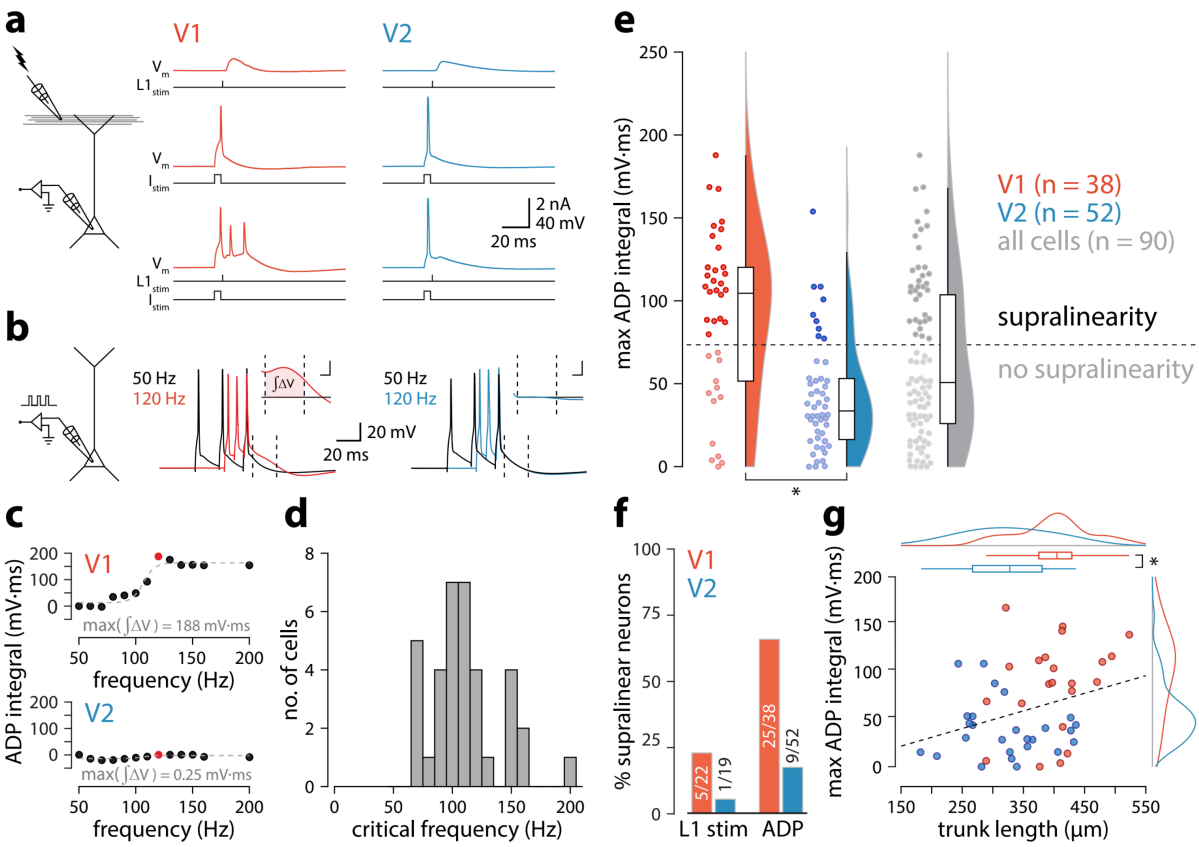

Figure 1. ttL5 neurons in V2m are less prone to burst than in V1.

a. *Left:* diagram of experimental configuration. Somatic whole-cell patch-clamp recording electrode and extracellular stimulation electrode in L1. *Right:* example traces from V1 (red) and V2m (blue) ttL5 neurons. **b.** *Left:* diagram of experimental configuration. Somatic whole-cell patch-clamp electrode evoking 3 APs. *Right:* example traces of V1 (red) and V2m (blue) ttL5 neurons stimulated with 50 Hz and 120 Hz AP trains. Note the sustained after-depolarization following the 120 Hz spike train in the V1 neuron. *Inset:* ADP measured as the area between the 50 Hz trace and the higher frequency trace following the last spike. Inset scale bar: 5 ms x 5 mV. **c.** Quantification of ADP area at each measured frequency for the example neurons in *b*. The peak integral value is highlighted in red. **d.** Histogram of critical frequencies across all recorded cells in both V1 and V2m. Cells with no identifiable critical frequency were excluded from this plot. **e.** Summary data of peak ADP integral values for every recorded neuron in V1 and V2m. The dashed line indicates the division between the two groups of cells classified through k-means clustering, drawn halfway between the cell with the lowest maximum ADP in the "supralinearity" cluster and the cell with the highest value in the "no supralinearity" cluster. **f.** Proportion of recorded bursting cells in V1 and V2m measured in the experimental configurations described in *a* and *b*. **g.** Length of the apical trunk (soma to main bifurcation) plotted against the corresponding maximum ADP integral values. Dashed line is a linear fit; curves at the top and right are kernel density plots of the two variables in V1 and V2m. All boxplots in the figure show the median, interquartile range, minimum and maximum values of the dataset.

BAC firing is absent in short ttL5 models

To investigate the possible mechanisms underlying the dependence of bursting on apical trunk length, we ran numerical simulations in conductance based compartmental models of ttL5 neurons. We first probed BAC firing in a morphologically detailed model published by Hay et al (2011), using the model parameters (biophysical model 3) and morphology (cell #1) favoured for reproducing BAC firing. As in the original paper, BAC firing was triggered by injecting a 0.5 nA current at the apical bifurcation coupled to a somatic action potential evoked by square-pulse current injection at the soma. Mirroring the responses seen in the subset of strongly bursting ttL5 neurons, coincident stimulation triggered BAC firing in this detailed model (**Fig. 2a, left**), as has previously been shown. We then applied the same model to a different ttL5 morphology with a shorter apical dendrite, reconstructed from one of our previously recorded V2m cells. The only parameter adjustment made to the detailed model when applying it to our shorter morphology was to re-specify the location of the Ca^{2+} channel hot spot around the new apical branch point (350–450 µm from the soma). The amplitude of the dendritic current injection in the short morphology (0.194 nA) was also scaled so as to obtain the same depolarization amplitude at the bifurcation in both model cells. With this morphology, coincident tuft and somatic stimulation evoked only a single somatic spike and did not trigger a dendritic Ca^{2+} plateau (**Fig. 2a, right**). To test if the short neuronal morphology was capable of showing Ca^{2+} plateaus, we stimulated the short neuron with 0.5 nA at the dendritic electrode. While the resulting dendritic potential was substantially larger, this resulted in only a small depolarization at the soma, and even when combining it with a somatic spike it did not trigger a burst of spikes (**Supplementary Figure 2.1**).

The morphologically detailed models contained two Ca^{2+} conductances—low-voltage activated and high-voltage activated—clustered in an area around the apical branch point, which are responsible for the dendritic Ca^{2+} plateau potential. To explore the sensitivity of Ca^{2+} plateaus to the dendritic Ca^{2+} channel density in the long and short neurons, we scaled the Ca^{2+} conductance (g_{Ca}) between 0 and 8 times the original values. To minimize the number of variables, when scaling the relative g_{Ca} we kept the ratio of the two channels constant. In the long morphology the integral of the distal dendritic voltage, acting as an indicator of the large and sustained depolarization during a Ca^{2+} plateau, increased proportionally to g_{Ca}. In the short morphology, however, this value stayed constant across all g_{Ca} values (**Fig. 2b**). This indicates that, although the size of a Ca^{2+} plateau depends on g_{Ca} in long neurons, in short neurons there is no Ca^{2+} channel activation and the magnitude of the voltage integral therefore does not depend on g_{Ca}.

Biophysical models with detailed long and short morphologies thus were able to reproduce the results from our experiments. To more easily manipulate the dendritic length across a continuous range of values, we investigated the same phenomenon in a reduced ttL5 model based on Bahl et al (2012). The simplicity of this model has the added benefit of reducing the number of variables, allowing us to more easily identify general principles of dendritic voltage propagation. One notable difference in this simplified model is that Ca^{2+} channels are all located in the tuft compartment, rather than being in a hot spot around the bifurcation. The tuft in this model should therefore be considered equivalent to a combination of the bifurcation and apical tuft dendrites.

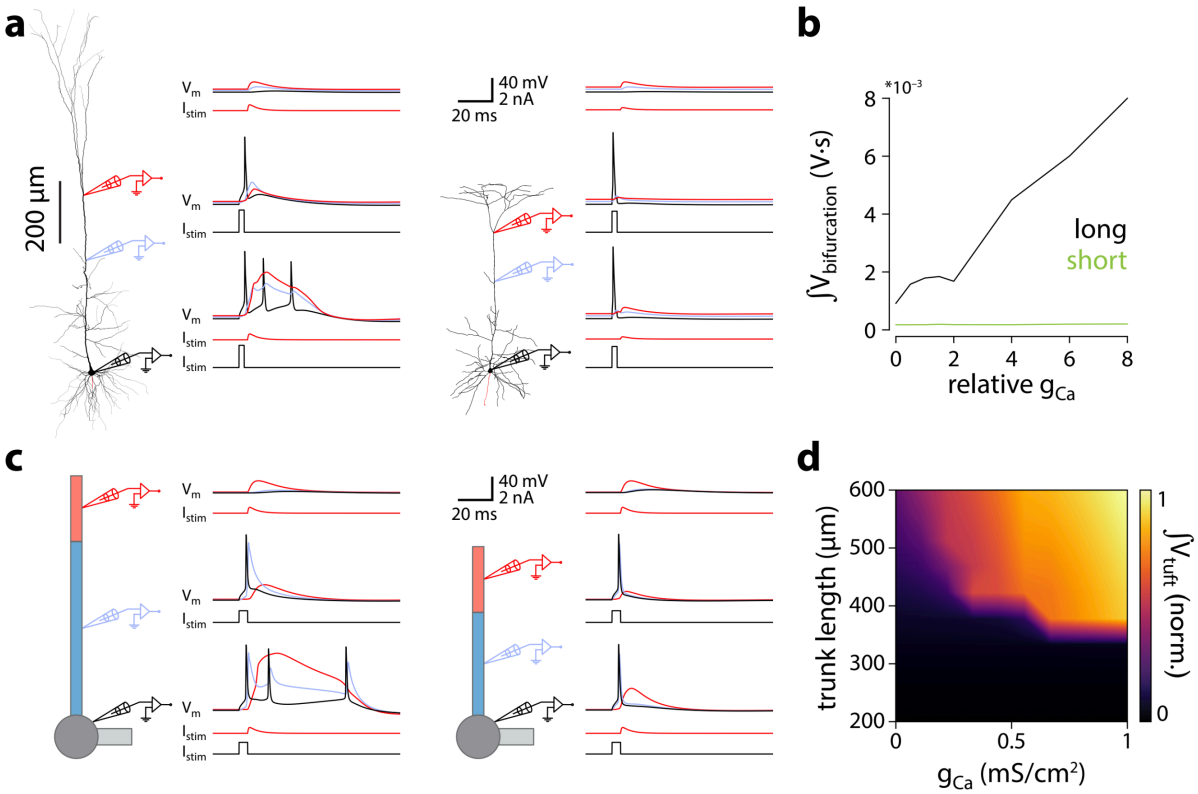

Figure 2. Shorter model neurons are less prone to burst.
a. *Left:* detailed morphology of a ttL5 pyramidal neuron from the model favoured by Hay et al. (2011) for reproducing BAC firing. *Right:* reconstructed morphology from a recorded ttL5 neuron in V2m. For each cell, injected current and voltage traces are shown for the soma (black), the apical trunk (blue, 400 and 200 µm), and the main bifurcation (red, 620 and 370 µm) under three different stimulation paradigms. **b.** Integral of voltage at the branch point in the long and short model neuron during combined somatic and branch point stimulation, plotted against the relative g_{Ca}. **c.** *Left:* diagram of the reduced model neuron. The length of the apical trunk in this model was 800 µm. Voltage traces are given for three different stimulation paradigms, with recordings made at the centres of the somatic compartment (black), apical trunk compartment (blue), and tuft compartment (red). *Right:* the same current and voltage traces are shown for a version of the Bahl model modified to have an apical trunk length of 200 µm. **d.** Heat map representing the normalised tuft voltage integral during combined somatic and tuft stimulation in the reduced model, plotted against the absolute density of Ca^{2+} channels in the tuft compartment and the length of the apical trunk compartment. Default $g_{Ca} \cong 0.45$ mS/cm^2.

As with the morphologically detailed model, the reduced model with the original published parameters displays BAC firing triggered by coincident tuft and somatic stimulation (**Fig. 2c, left**). Shortening the apical trunk was sufficient to eliminate this response (**Fig. 2c, right**). We explored the dependence of BAC firing on apical trunk length and calcium conductance while measuring the time-integral of tuft voltage as an indicator of Ca^{2+} plateau potentials (**Fig. 2d**). The presence of a Ca^{2+} plateau depended strongly on apical trunk length and was only sensitive to g_{Ca} above a critical length of approximately 350 µm ($\cong 0.35\ \lambda$). Below this length, no Ca^{2+} plateaus were triggered regardless of how high g_{Ca} was set to. These experiments show that a simplified model also reproduces our results, allowing us to explore and dissect the underlying parameters in more detail.

Active propagation enhances voltage in long dendrites

To obtain a mechanistic understanding of what causes the length dependence of bursting, we made recordings from the final segment of the apical trunk as well as the apical tuft using the reduced model. To recreate the experimental conditions of **Fig. 1b**, we triggered 3 spikes at 100 Hz through a somatic electrode. Similarly to coincident bAP and tuft input, increasing the length of the apical trunk facilitated dendritic Ca^{2+} plateau initiation (**Fig. 3a**). Upon closer inspection, the width and peak voltage in the tuft steadily increased with dendritic length (**Fig. 3b,c**), even in the absence of Ca^{2+} currents ($g_{Ca} = 0$). In the presence of voltage-gated Ca^{2+} channels, this increased amplitude of bAPs triggered a larger all-or-none Ca^{2+} plateau above a certain threshold length.

We found that bAP amplitude in the tuft increased as a function of apical trunk length despite a decreasing bAP amplitude in the distal segment of the trunk (**Fig. 3b**). We also observed that the width of the bAP (measured 2 mV above baseline) increased with length in both the tuft and trunk (**Fig. 3c**). While waveform broadening is a natural consequence of passive filtering along dendrites, the sustained voltage in the distal trunk required active dendritic propagation. In the reduced model, this active propagation in the apical trunk was mediated primarily by voltage-gated Na^{+} channels. Removing these channels caused a substantial reduction in peak voltage and width of the depolarization in the distal trunk, and importantly also abolished the trend of increasing tuft voltages with longer dendritic trunks (**Fig. 3d,e**). More generally, active propagation caused bAPs to be larger and broader at all distances along a long dendrite compared to the same absolute distances in shorter dendrites (**Supplementary Figure 3.1**). Because of this, when comparing the final positions along the trunk, the peak voltage is only marginally smaller in long dendrites despite the larger distance from the soma. This is not the case in a passive dendrite, where voltage attenuation depends primarily on distance and is not sensitive to trunk length. The general phenomenon of enhanced voltage propagation in longer dendrites resulting in amplification of tuft voltage was not sensitive to the specific distribution of active conductances implemented in this model. When all conductances were uniformly distributed along the apical trunk the waveforms did not substantially change and the enhanced voltage continued to trigger Ca^{+} plateaus only in neurons with long apical trunks (**Supplementary Figure 3.2**).

While it might seem counterintuitive that peak voltage in the tuft increases when the peak trunk voltage is decreasing, we propose that the increasing width of the depolarization can at least partially account for this via a passive mechanism. Wider depolarizations allow the tuft compartment to charge to a higher voltage. The rate and peak value of tuft charging depends on the passive properties of the tuft. The peak value of depolarization reached and the rate of voltage change are proportional to membrane resistance (R_m) and membrane capacitance (C_m), respectively. The product of these two parameters gives the membrane time constant (τ). To illustrate this, we applied voltage-clamp to the end of the distal segment of the trunk and delivered 30 mV square voltage pluses of increasing width (**Fig. 3f**). Due to the capacitive filtering of the tuft, short voltage steps did not fully charge the tuft while wide voltage steps allowed the tuft voltage to reach the steady-state values commanded by R_m. To directly test the hypothesis that the relationship between trunk depolarization width and tuft membrane time constant caused the bAP amplitude in the tuft to increase with length, one could vary R_m by changing g_{leak}. However, this would affect resting membrane potential and consequently alter voltage-dependent properties of the tuft. We therefore chose to vary C_m instead, in order not to affect other variables in the model. For a given value of depolarization amplitude and width, increasing C_m (and therefore τ) in the tuft caused a reduction in the peak tuft voltage (**Fig. 3g**). These simulations show that the tuft time

constant and the width of the bAP interact to create a higher tuft depolarization with longer apical trunks.

It has previously been suggested that axial resistance (R_a) in the apical dendrite may influence the backpropagation efficiency in dendrites and burstiness of ttL5 neurons (Fletcher & Williams 2019). To test this hypothesis, we measured peak voltage and width in the trunk and tuft for different trunk lengths under different R_a conditions. We found that peak tuft voltage (and therefore burstiness) increased with increasing trunk R_a, reaching the highest voltage near the reduced model's original value of R_a, and decreasing again for higher values of R_a (**Supplementary Figure 3.3**). However, in these simulations burstiness always increased with trunk length regardless of R_a. This indicates that, although important, it was not the primary determinant for generating the length-dependent effect.

Overall, the combination of increased width and a relatively small reduction in amplitude resulted in a trunk voltage integral that increased with trunk length, thereby passing more charge to the adjacent tuft compartment. However, if active backpropagation was reduced or absent, the trunk integral and resulting tuft voltage decreased with length (**Fig.3d,e**). The peak tuft voltage approximately followed the integral of voltage in the distal trunk. To illustrate this, we applied voltage-clamp to the end of the trunk and injected square steps with a range of integrals obtained through various combinations of width and amplitude (**Fig. 3h**). This revealed a zone above a critical trunk integral for which many different width and depolarization combinations were sufficient to evoke a Ca^{2+} plateau in the tuft (**Fig. 3i**).

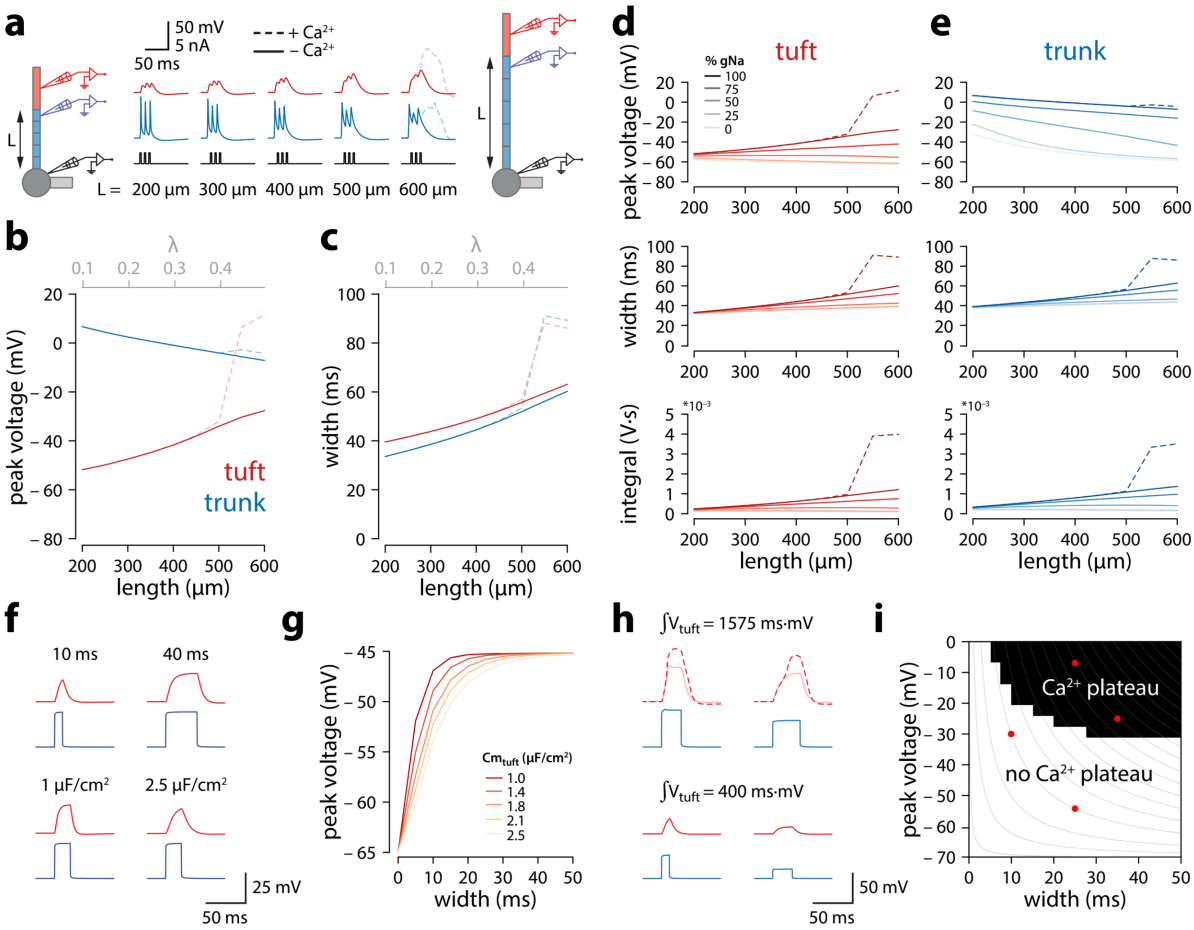

Figure 3. Tuft voltage increases with trunk length due to the widening of bAPs.
a. Schematic of the simulation: stimulation site in the somatic compartment, and recording sites at the distal end of the apical trunk (blue) and in the centre of the tuft (red). Stimulus shown in black. Solid lines: $g_{Ca} = 0$; dashed lines: original g_{Ca}. **b.** Peak voltage reached in trunk (blue) and tuft (red) for a range of simulations with different trunk lengths, using the same stimulation protocol as in *a*. **c.** Same as in *b*, but plotting the width of the depolarization measured 2 mV above baseline. Length constant $\lambda = 1009$ µm. **d,e.** Peak voltage, width and integral values measured in the trunk and tuft for dendrites containing different Na^+ channel densities in the apical trunk (as a percentage of the original values). **f.** Example traces during voltage-clamp of distal trunk. Voltage steps were delivered in the trunk (blue) under differing tuft membrane capacitance conditions and the tuft voltage (red) was recorded. **g.** Peak voltage values reached in the tuft for a range of trunk step widths and tuft capacitances. In the original model, tuft $C_m \cong 1.75$ µF/cm^2. **h.** Same as in *f*, but showing voltage steps of different width and amplitude with the same voltage integral in the trunk. For large integrals (top), the tuft voltage crosses the threshold for a Ca^{2+} plateau, while for smaller integrals (bottom) the voltage remains subthreshold. **i.** Voltage and width combinations for square voltage steps in the distal trunk which result in a Ca^{2+} plateau in the tuft. Red points represent the values used in *h*. Grey lines indicate width and amplitude combinations with equal integral.

Discussion

While much is known about the Ca^{2+}-mediated supralinearities of ttL5 neurons (Groh et al 2010, Kasper et al 1994, Kim et al 2015, Larkum 2013, Ramaswamy & Markram 2015), our existing knowledge is mainly based on experiments done in V1 and primary somatosensory cortex of 4-8 week old rats. Previous studies often selected cells based primarily on soma size and approximate shape of the dendrites, potentially introducing biases in the selection which could skew the results towards specific subtypes of L5 neurons. This may be particularly relevant in light of recent evidence showing that there are functional differences between different projection-defined populations in L5 (Kim et al 2015, Lur et al 2016). We have sought to overcome some of these limitations by selecting cells using more easily reproducible criteria. We selected cells in L5 uniformly based on either their expression of Glt25d2-Cre (a ttL5-specific line, Groh et al 2010) or on their projection to the lateral posterior (LP) thalamic nucleus, which we determined using retrograde CTB labelling. In the subset of the recorded neurons which were successfully filled with biocytin, we were able to confirm that these cells also had the characteristic morphological features of ttL5 neurons. We were thus able to maintain cortical area as the primary variant when comparing V1 and V2m neurons.

Our results show that, contrary to common assumptions, there are considerable differences in the properties of ttL5 neurons across different brain regions. Indeed, both BAC firing and critical frequency ADP, which are considered hallmarks of dendritic Ca^{2+} plateaus, were found to be less common in V1 than we anticipated based on the results from rat somatosensory cortex, and were almost completely absent in V2m. Since in our experiments BAC firing was evoked by extracellular stimulation of axons in L1, it is possible that part of the observed difference between V1 and V2m was due to different amounts of inhibition recruited by this type of stimulation. However, this would not explain the differences measured with the critical frequency paradigm, as these Ca^{2+} plateaus were evoked solely by intracellular stimulation of the soma and were therefore less likely to be affected by the recruitment of polysynaptic inhibitory circuits. This evidence presents an argument against the commonly cited notion that the neocortex is composed of canonical circuits performing the same computations on different sets of inputs across the brain (Douglas & Martin 2004, Harris & Shepherd 2015, Hawkins et al 2019, Jiang et al 2015, Markram et al 2015, Miller 2016, Mountcastle 1997). Instead, it implies that the non-linear computations performed through Ca^{2+} plateaus and BAC firing may not be required in more associative areas outside of the primary sensory cortices, perhaps because in these regions the cortical hierarchy is less defined. It may therefore be more important to maintain equal weighting between different sensory modalities and rely on other mechanisms to change the weights according to the reliability of each input.

Although all cells were selected according to the same criteria, we found that the ttL5 neurons in V2m had significantly shorter apical trunks than the V1 neurons. This is consistent with recent structural MRI data showing a reduced neocortical thickness in the most caudal and medial portions of the rodent brain (Fletcher & Williams 2019). Using an existing biophysical ttL5 model, which was designed to reproduce classic ttL5 properties such as BAC firing (Hay et al 2011), we found that the same model applied to a morphology with a shorter apical trunk resulted in a loss of BAC firing independently of Ca^{2+} channel density. To determine the subcellular dynamics causing this effect, we moved to a reduced ttL5 model with a simplified morphological structure (Bahl et al 2012) that could be more easily manipulated and where the effects would be more interpretable. As in the morphologically detailed model, the BAC firing response which was present in the original model disappeared when shortening the apical trunk. Because of the structural simplicity of this model, we were able to study this effect

across a wide range of trunk lengths and thereby identify a sharp length cut-off at around 0.35 λ (≅ 350 μm in model space), below which BAC firing was abolished. A notable simplification in the reduced model is that the apical trunk and oblique dendrites are compressed into the same compartment. The model parameter fits were also based on recordings from rat neurons. Therefore, the numerical values of model length do not translate directly into apical trunk lengths for real mouse neurons. It is also worth noting that, as the reduced model does not have a distinct compartment to represent the apical bifurcation (where the Ca^{2+} channel hot spot is located in the morphologically detailed model), all Ca^{2+} channels are placed in the tuft compartment.

As backpropagation from the soma into the dendrites is a key aspect of BAC firing, we investigated this aspect more closely by recording the dendritic voltage in response to backpropagating somatic spikes in models with different apical trunk lengths. Surprisingly, we found that the voltage in the tuft did not attenuate, but rather increased as a function of trunk length. This was in contrast to the trunk voltage, whose peak did indeed attenuate with increased distance from the soma. We were able to demonstrate that the tuft amplification depended on a sustained broadening depolarization in the distal trunk which was generated by voltage gated Na^+ channels present along the trunk. While this broadening was proportional to trunk length, the Na^+ channel activation reduced the attenuation of spike amplitude over distance. The combined effect of these changes caused neurons with a longer apical trunk to have a greater voltage integral in the trunk, leading to greater charging of the tuft. We hypothesise that, above a minimal threshold for peak trunk voltage, the primary determinant of peak tuft voltage is the time-averaged voltage in the trunk. Supporting this view, we found that many different combinations of depolarization width and amplitude in the trunk could trigger Ca^{2+} plateaus. It is interesting to note that, in the presence of Na^+ channels, the bAP at any given absolute distance from the soma was larger and broader in neurons with longer trunks. This may be due to a cooperative effect of each trunk section on the sections both up- and downstream, with the voltage at each location decaying slower because of the more depolarised state of the remaining dendrite. This observation could potentially be verified experimentally with dendritic recordings by comparing the bAP width and amplitude at equivalent absolute distances from the soma in neurons with long and short apical dendrites. It would also be possible to measure the voltage at the apical bifurcation in response to a train of bAP in the presence of Ca^{2+} channel blockers, in order to determine if the voltage profile at the Ca^{2+} hot spot is indeed different in long neurons.

Axial resistance in the apical dendrite is another important factor influencing the electrical coupling to the soma and has been suggested to be involved in determining a difference in BAC firing between anterior and posterior V1 neurons (Fletcher & Williams 2019). While we did see a decrease in tuft voltage when reducing the trunk R_a, the voltage was always larger in the neurons with longer trunk, showing that the effects of variations in R_a and trunk length are independent. If R_a indeed correlates with length, these effects may combine to further enhance the tuft voltage in long neurons.

One notable counterexample to the principle that long neurons should be more prone to burst through enhanced backpropagation is the human ttL5 neuron, which was recently shown to have greater compartmentalization and reduced excitability compared to rat neurons, despite being substantially longer (Beaulieu-Laroche et al 2018). However, this may still be consistent with our predictions as the paper also reports reduced ion channel densities in human ttL5 neurons, which we show to be crucial for the length-dependent enhancement. Furthermore, as the boosting effects of a broader depolarization are subject to saturating (when the depolarization is wide enough to fully charge the tuft), we would

predict that the positive effect of length on tuft voltage does not increase monotonically, as above a certain apical trunk length the trunk voltage would attenuate to the point where it is no longer sufficient to trigger a Ca^{2+} plateau.

In conclusion, we have characterised previously undescribed key differences in the intrinsic integrative properties of ttL5 neurons in V1 and V2m. Our results contribute new insights on the diversity of ttL5 neurons and on the possible mechanisms through which morphology can influence their integrative properties, adding to the growing body of evidence that the properties and canonical computations of cortical circuits across the brain may not be as stereotyped as is commonly believed. This cellular heterogeneity may functionally expand the ability of cortical areas to specialize in the computations that are required for processing their particular set of inputs, at the cost of reduced flexibility in generalizing to other types of input.

Materials and Methods

Animals

All animal experiments were prospectively approved by the local ethics panel of the Francis Crick Institute (previously National Institute for Medical Research) and the UK Home Office under the Animals (Scientific Procedures) Act 1986 (PPL: 70/8935). Wild-type and transgenic male mice were used. Tg(Colgalt2-cre)NF107Gsat (Glt, MGI:5311719) and Tg(Rbp4-cre)KL100Gsat (Rbp, MGI:4367067) lines created by the Gensat project (Gerfen et al 2013, Groh et al 2010) were crossed with the Ai14 reporter line expressing tdTomato (MGI:3809524). Animals were housed in individually ventilated cages under a normal 12-hour light/dark cycle.

Surgical procedures

Surgeries were performed on mice aged 3–7 weeks using aseptic technique under isoflurane (2–4%) anaesthesia. Following induction of anaesthesia, animals were subcutaneously injected with a mixture of meloxicam (2 mg/kg) and buprenorphine (0.1 mg/kg). During surgery, the animals were head-fixed in a stereotactic frame and a small hole (0.5–0.7 mm) was drilled in the bone above the injection site. Alexa Fluor 488-conjugated Cholera toxin subunit B (CTB, 0.8% w/v, Invitrogen) was injected using a glass pipette with a Nanoject II (Drummond Scientific) delivery system at a rate of 0.4 nL/s. Injections of 100–200 nL were targeted to the lateral posterior (LP) thalamic nucleus, with stereotactic coordinates: 2.2–2.5 mm posterior to bregma, 1.45 lateral of the sagittal suture, 2.45 mm deep from the cortical surface. To reduce backflow, the pipette was left in the brain approximately 5 minutes after completion of the injection before being slowly retracted.

Slice preparation

Male mice (6–12 weeks old) were deeply anaesthetised with isoflurane and decapitated. In mice that were injected with CTB, this occurred at least 3 weeks after the injection. The brain was rapidly removed and placed in oxygenated ice-cold slicing ACSF containing (in mM): 125 sucrose, 62.5 NaCl, 2.5 KCl, 1.25 NaH_2PO_4, 26 $NaHCO_3$, 2 $MgCl_2$, 1 $CaCl_2$, 25 dextrose; osmolarity 340–350 mOsm. Coronal slices (300 µm thick) containing visual cortex were prepared using a vibrating blade microtome (Leica VT1200S or Campden 7000smz-2). Slices were immediately transferred to a submerged holding chamber with regular ACSF containing (in mM): 125 NaCl, 2.5 KCl, 1.25 NaH_2PO_4, 26 $NaHCO_3$, 1 $MgCl_2$, 1.5 or 2 $CaCl_2$, 25 dextrose; osmolarity 308–312 mOsm. The holding chamber was held in a water bath at 35 °C for the first 30–60 min after slicing, and was kept at room temperature (22 °C) for the remaining time (up to 12 hours) after that. All solutions and chambers were continuously bubbled with carbogen (95% O_2 / 5% CO_2).

Electrophysiology

After the 35 °C incubation period, individual slices were transferred from the holding chamber to the recording chamber, where they were perfused at a rate of ~6 mL/min with regular ACSF (see above) continuously bubbled with carbogen and heated to 35 ± 1 ℃. Borosilicate thick-walled glass recording electrodes (3-6 MΩ) were filled with intracellular solution containing (in mM): 115 CH_3KO_3S, 5 NaCl, 3 $MgCl_2$, 10 HEPES, 0.05 EGTA, 3 Na_2ATP, 0.4 NaGTP, 5 K_2-phosphocreatine, 0.5% w/v biocytin hydrochloride (Sigma), 50 µM Alexa Fluor 488 hydrazide (Invitrogen); osmolarity 290-295 mOsm; pH 7.3. Visually guided whole-cell patch-clamp recordings were targeted to neurons in L5 of medial V2 (V2m) and V1 that were fluorescently labelled with either CTB or with tdTomato (for Glt25d2-Cre mice), to ensure that the recordings were restricted to ttL5 neurons. Visual areas were defined based on

approximate stereotactic coordinates (as defined in Franklin & Paxinos 2007). All recordings were made in current-clamp mode. Extracellular monopolar stimulation was achieved by passing a DC current pulse (0.1-1 ms, 20-320 µA) through a glass patch-clamp pipette with a broken tip (~20 µm diameter) using a constant current stimulator (Digitimer DS3). Current was passed between two chlorided silver wires: one inside the pipette, which was filled with recording ACSF, and the other coiled around the outside of the pipette.

Immunohistochemistry and morphological reconstructions

After recording, slices were fixed overnight at 4 °C in a 4% formaldehyde solution and were subsequently kept in PBS. For immunohistochemical detection, the fixed slices were first incubated for 1-2 hours at room temperature in blocking solution containing 0.5% Triton X-100 and 5% Normal Goat Serum (NGS) in PBS. Slices were then washed twice (10 min each) in PBS and incubated overnight in a staining solution containing 0.05% Triton X-100, 0.5% NGS, DyLight 594-conjugated streptavidin (2 µg/ml). Slices were then washed in PBS (3 times, 5 min each) and stained with DAPI (5 µg/ml) for 10 min. After another wash (3 times, 5 min each), slices were mounted on glass slides and images were acquired with a confocal microscope (Leica SP5, objective: 20x/0.7NA or 10x/0.4NA, pinhole size: 1 airy unit). The images were used to reconstruct the neurons with Neurolucida 360 (MBF bioscience).

Data acquisition and analysis

Electrophysiological data were acquired with a Multiclamp 700B amplifier (Molecular Devices) and digitised through a National Instruments DAQ board (PCIe-6323). Recordings were Bessel-filtered at 8 kHz before digitization with 20 kHz sampling. Offline analysis was performed with custom scripts in Matlab (Mathworks) and Igor Pro (Wavemetrics).

Modelling

Simulations were performed with the NEURON simulation environment (7.7.1, Carnevale & Hines, 2006) embedded in Python 3.6. To model the consequences of morphological differences between V1 and V2m ttL5 cells, we utilised existing models of ttL5 pyramidal cells with either accurate morphological detail (biophysical model 3, cell #1 from Hay et al 2011, referred to as detailed model) or simplified multicompartment morphologies (Ca^{2+} enriched model 2 from Bahl et al 2012, referred to as reduced model). To study the effect of morphology in the detailed model, biophysical model 3 from (Hay et al 2011) was applied to the reconstructed morphology from one of our recorded ttL5 neurons in V2m (which has a substantially shorter apical trunk than the morphology used in the original model). Each morphology contained low-voltage-activated (LVA) and high-voltage-activated (HVA) Ca^{2+} channels located in a region around the main apical bifurcation. This region was 685–885 µm from the soma in the long morphology (cell #1 from Hay et al 2011) and 350–450 µm in the short morphology.

Subsequent simulations using the reduced model were done by modifying only selected parameters described in the results, such as the length of the apical trunk compartment, leaving all other parameters unchanged. Briefly, this reduced model (Bahl et al 2012) is divided into sections representing the soma, axon (hillock and initial segment, AIS), basal dendrites, apical trunk, and apical tuft. Active conductances are present in all compartments and include the following: hyperpolarization-activated cation (HCN) channels (basal dendrite, apical trunk, tuft), transient voltage-activated Na^+ (Na_t) channels (soma, axon hillock, AIS, apical trunk, tuft), persistent voltage-activated Na^+ (Na_p) channels (soma), fast voltage-activated K^+ (K_{fast}) channels (soma, apical trunk, tuft), slow voltage-activated K^+ (K_{slow}) channels (soma, apical trunk, tuft), muscarinic K^+ (K_m) channels (soma), slow Ca^{2+} (Ca_s) channels (tuft), Ca^{2+} dependent K^+(K_{Ca}) channels (tuft), and a Ca^{2+} pump (tuft). The density of the K_{fast} and K_{slow}

channels decays exponentially from the soma to the tuft. The density of Na_t channels decays linearly from the soma to the tuft, while HCN channels linearly increase in density. N.B. the tuft, but not the trunk, contains Ca^{2+} channels; consequently there is no hot spot similar to the apical bifurcation in the detailed model. When varying trunk length, Na_t, K_{fast}, K_{slow}, and HCN conductances in each trunk segment were redistributed so as to take into account the new distance of each segment from the soma (thereby changing the total conductance in the trunk).

Acknowledgements
We thank Arnd Roth and Alexandra Tran-Van-Minh for advice on modelling. We are grateful to Lee Fletcher, Arnd Roth and Alexandra Tran-Van-Minh for helpful comments on the manuscript.

Author contributions
A.R.G.: Designed and performed biological experiments, designed modelling experiments, analysed data, wrote the paper. A.L.: Designed and performed modelling experiments, analysed data. E.A.R.: Conceptualized the research and designed experiments, acquired funding, wrote the paper.
All authors discussed the results and implications and commented on the manuscript at all stages.

Funding
A.R.G. was recipient of a Boehringer Ingelheim Fonds PhD Scholarship and a PhD scholarship from the Francis Crick Institute. E.A.R. is jointly funded by Wellcome and the Royal Society through a Sir Henry Dale Fellowship (104285/B/14/Z).

Supplementary Figures

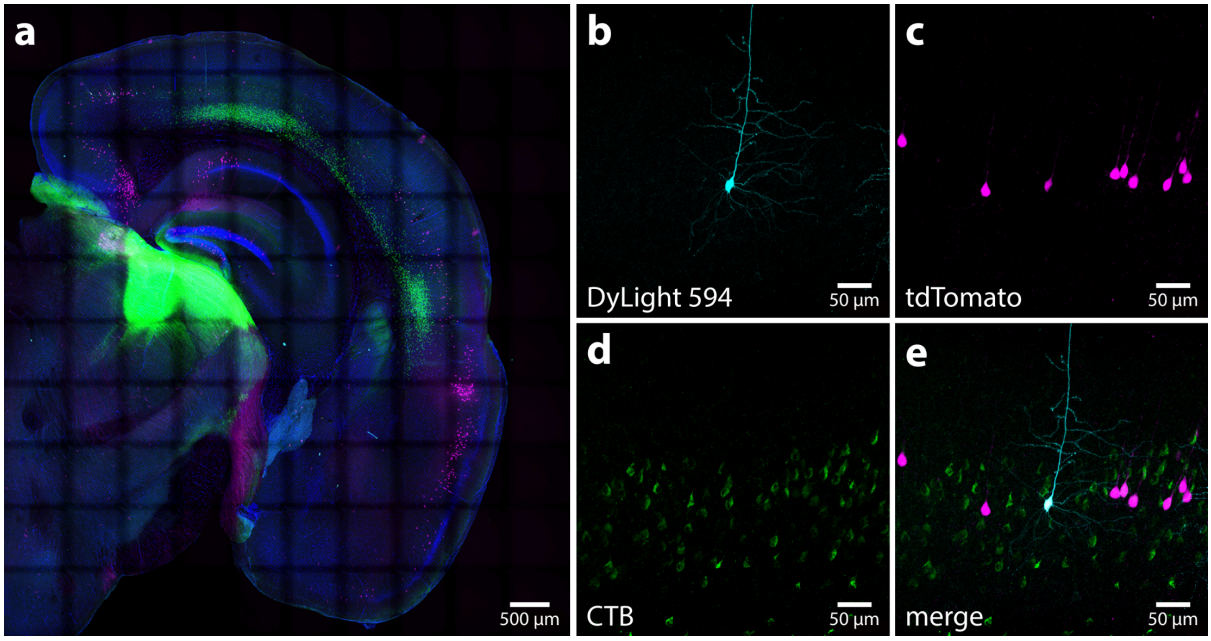

Supplementary Figure 1.1 Confocal images from a Glt25d2-Cre mouse injected with CTB-Alexa 488 in LP. a. Coronal slice of one hemisphere containing visual cortex, showing the injection site (green), tdTomato-expressing Glt25d2-Cre neurons (magenta), a DAPI stain (blue), and neurons that have been filled with biocytin during intracellular recordings and stained with DyLight 594 (cyan). **b.** Biocytin-filled ttL5 neuron in V2m. **c.** Neighbouring tdTomato-expressing Glt25d2-Cre neurons. **d.** CTB-labelled L5 neurons projecting to LP. **e.** Composite image of the above.

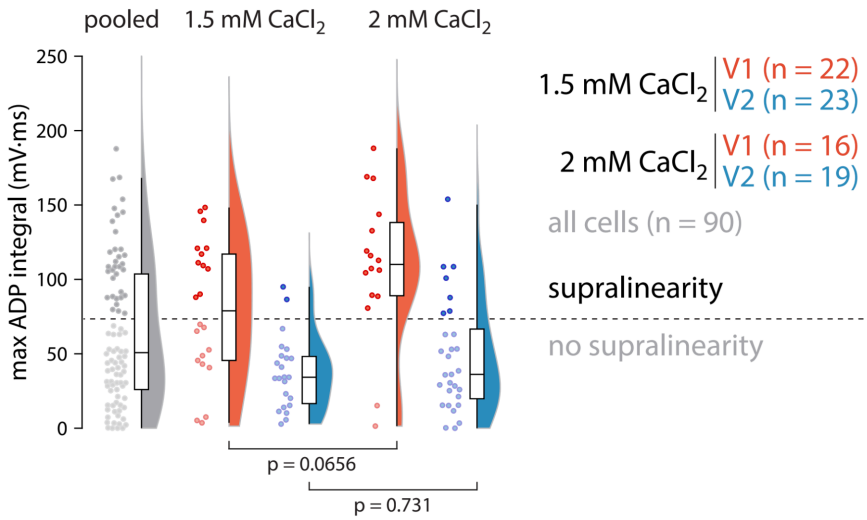

Supplementary Figure 1.2 Maximum ADP integral for all cells split by recording ACSF containing either 1.5 or 2 mM $CaCl_2$. Both V1 and V2m populations did not significantly differ between the two conditions ($p>0.05$, two sample t-test, two-tailed).

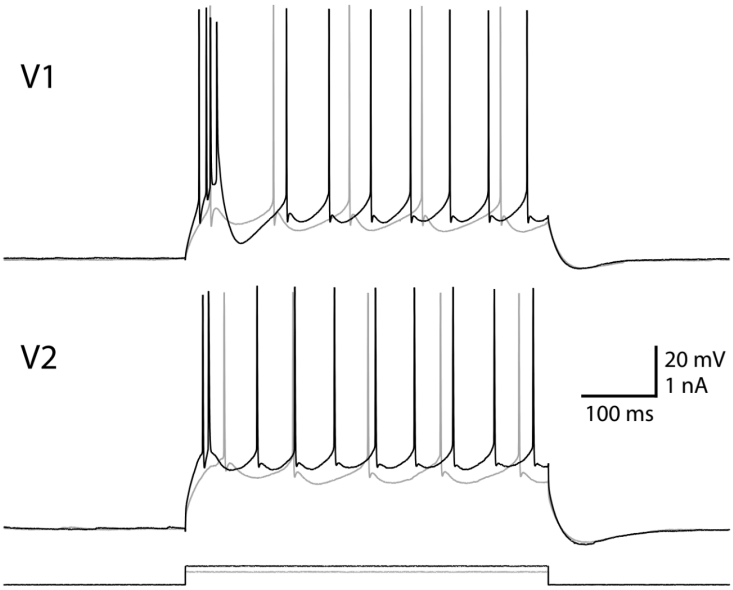

Supplementary Figure 1.3 Representative voltage traces for V1 and V2m neurons in response to 500 ms wide depolarizing current steps. The two example neurons were recorded from the same animal and both had the same rheobase (200pA). For each cell the traces show the responses to stimulation at 60 pA (grey line) and 180 pA (black line) above rheobase.

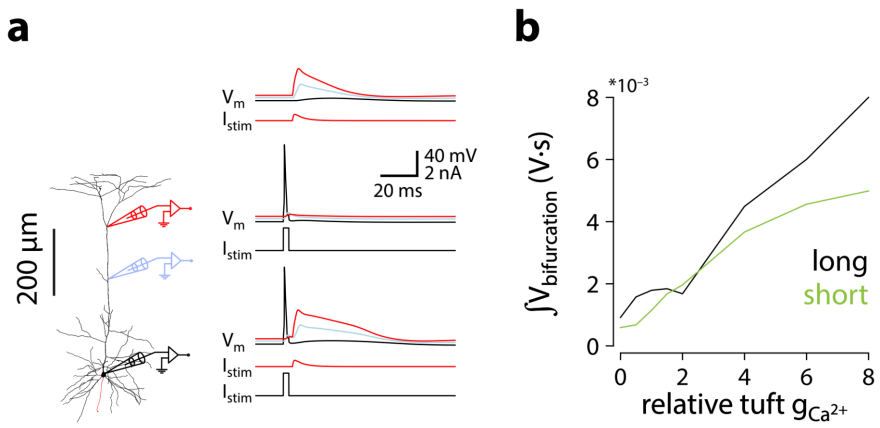

Supplementary Figure 2.1 Same as in *Fig. 2a & b*, but for the short morphology using the same dendritic current injection as in the long morphology (0.5 nA).

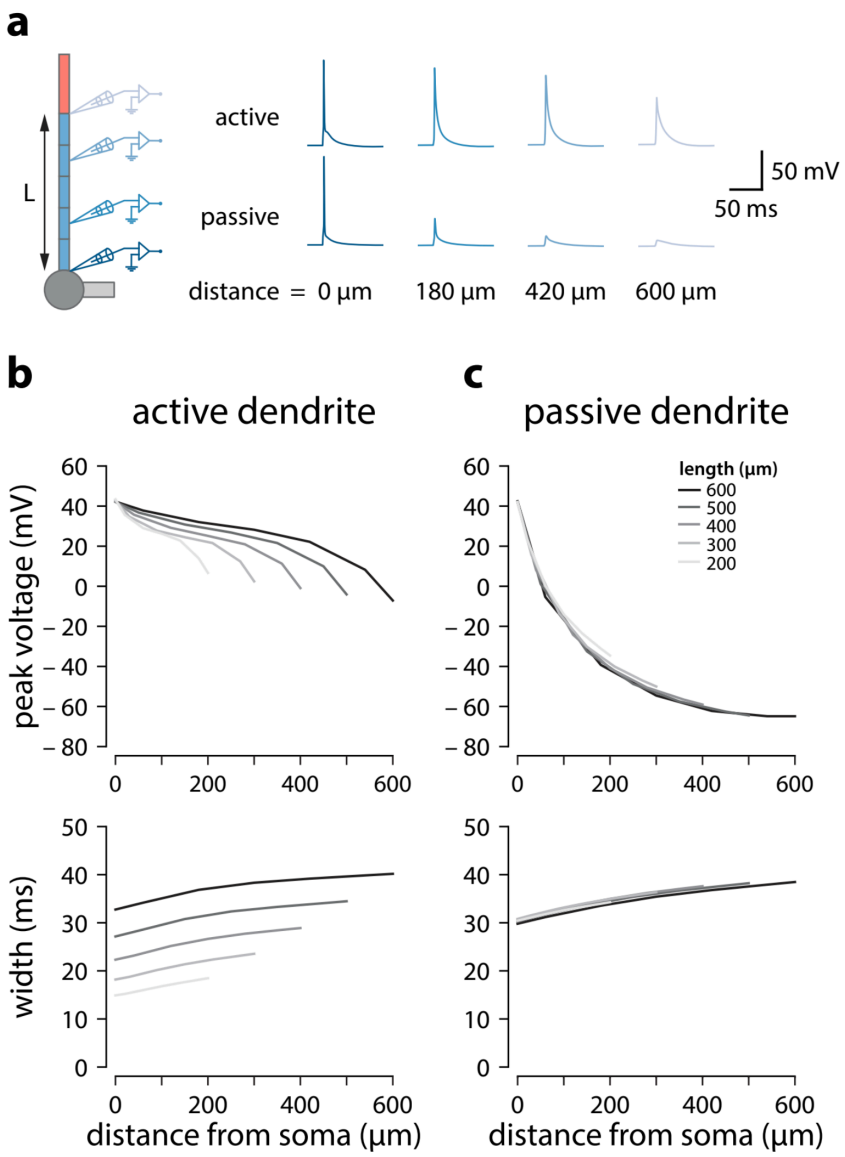

Supplementary Figure 3.1. Backpropagation of APs in active and passive trunks of different length. a. Backpropagation of a somatic spike elicited through a single 3 ms wide 2 nA square current step at the soma in a model neuron with 600 µm apical trunk length. Voltage recordings were made at different distances along the trunk. **b.** Peak voltage and width measured at different absolute distances (same relative) for active model neurons. Width was measured as the interval between the voltage values 2 mV above baseline membrane potential. Colours indicate models with different apical trunk lengths. N.B. At any given absolute distance from the soma, peak voltage and width of the bAP are larger when the apical trunk is longer. **c.** Same as in *b* but with all voltage-dependent conductances removed from the trunk and tuft compartments. N.B. voltage attenuation is independent of trunk length.

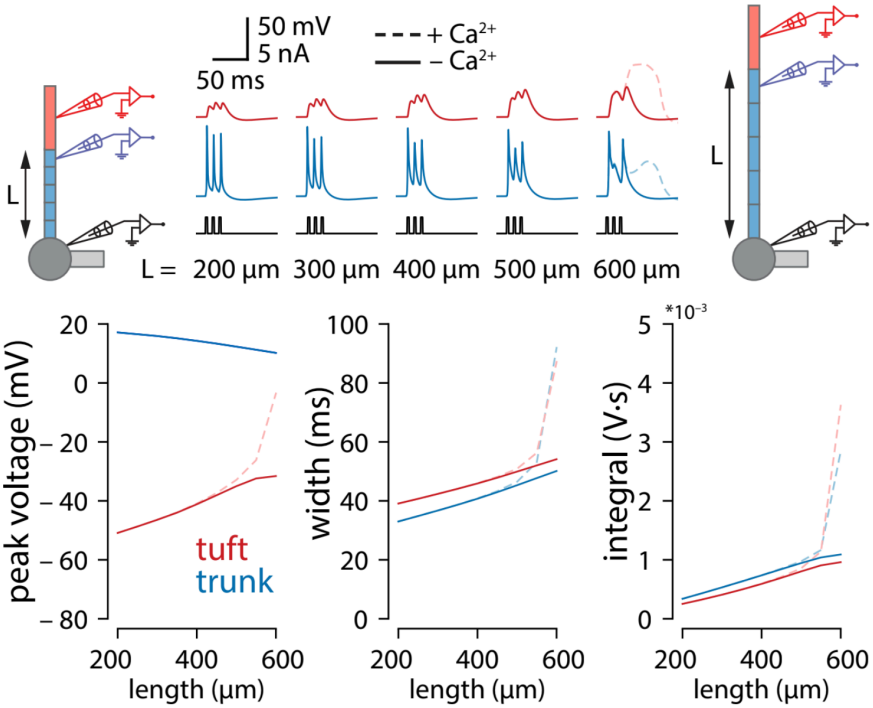

Supplementary Figure 3.2. Tuft voltage increases with trunk length independently of conductance gradients. Same experiments as in **Fig. 3a** but with uniform distribution of all active conductances in the apical trunk. Total conductance was maintained for each channel.

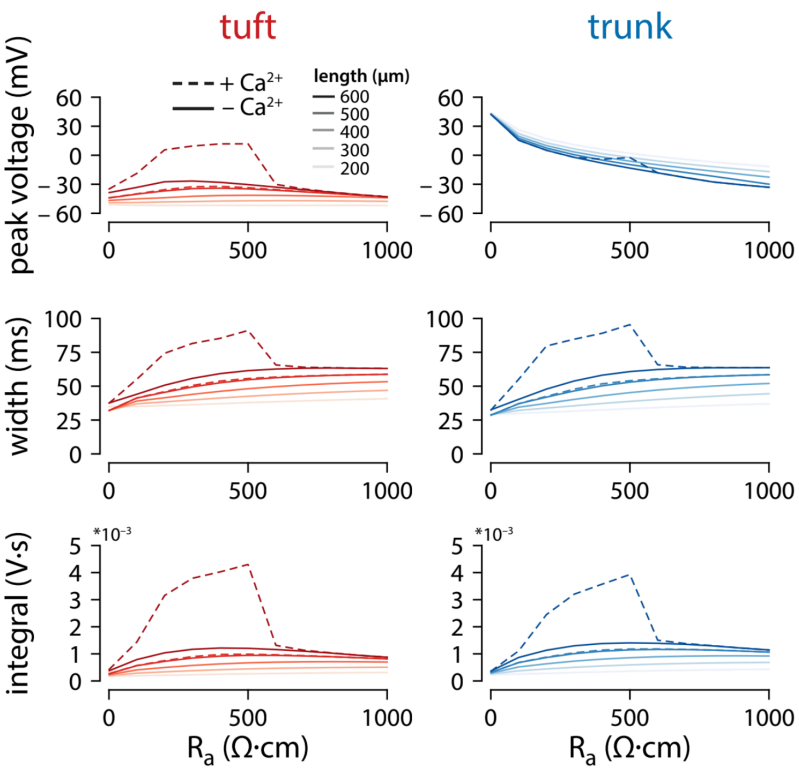

Supplementary Figure 3.3. Effect of axial resistance on voltage propagation. Plots of peak voltage, width, and voltage integral reached in the tuft and trunk for varying values of trunk length and axial resistance (R_a). Default $R_a \cong 382.22$ Ω·cm. The stimulus and recording conditions were the same as in **Fig. 2a**, with 3 APs at 100 Hz triggered in the somatic compartment. Solid lines show simulations with $g_{Ca} = 0$, while dashed lines show the same simulations with the original gCa = 0.45 mS/cm^2.

References

Amitai Y, Friedman A, Connors BW, Gutnick MJ. 1993. Regenerative Activity in Apical Dendrites of Pyramidal Cells in Neocortex. *Cereb Cortex* 3: 26-38

Bahl A, Stemmler MB, Herz AVM, Roth A. 2012. Automated optimization of a reduced layer 5 pyramidal cell model based on experimental data. *Journal of Neuroscience Methods* 210: 22-34

Bar M. 2006. A Cortical Mechanism for Triggering Top-Down Facilitation in Visual Object Recognition. http://dx.doi.org/10.1162/089892903321662976

Beaulieu-Laroche L, Toloza EHS, van der Goes M-S, Lafourcade M, Barnagian D, et al. 2018. Enhanced Dendritic Compartmentalization in Human Cortical Neurons. *Cell* 175: 643-51.e14

Beniaguev D, Segev I, London M. 2019. Single Cortical Neurons as Deep Artificial Neural Networks. *bioRxiv*: 613141

Cauller LJ, Clancy B, Connors BW. 1998. Backward cortical projections to primary somatosensory cortex in rats extend long horizontal axons in layer I. *Journal of Comparative Neurology* 390: 297-310

Clark A. 2013. Whatever next? Predictive brains, situated agents, and the future of cognitive science. *Behavioral and Brain Sciences* 36: 181-204

Coogan TA, Burkhalter A. 1990. Conserved patterns of cortico-cortical connections define areal hierarchy in rat visual cortex. *Exp Brain Res* 80: 49-53

Douglas RJ, Martin KAC. 2004. Neuronal Circuits of the Neocortex. *Annual Review of Neuroscience* 27: 419-51

Feldman H, Friston K. 2010. Attention, Uncertainty, and Free-Energy. *Front. Hum. Neurosci.* 4

Felleman DJ, Van Essen DC. 1991. Distributed hierarchical processing in the primate cerebral cortex. *Cereb. Cortex* 1: 1-47

Fletcher LN, Williams SR. 2019. Neocortical Topology Governs the Dendritic Integrative Capacity of Layer 5 Pyramidal Neurons. *Neuron* 101: 76-90.e4

Franklin KBJ, Paxinos G. 2007. *Paxinos and Franklin's The mouse brain in stereotaxic coordinates*. Amsterdam: Academic Press, an imprint of Elsevier. 1 volume (unpaged) pp.

Freedman DJ, Ibos G. 2018. An Integrative Framework for Sensory, Motor, and Cognitive Functions of the Posterior Parietal Cortex. *Neuron* 97: 1219-34

Friston K. 2008. Hierarchical Models in the Brain. *PLOS Computational Biology* 4: e1000211

Gerfen Charles R, Paletzki R, Heintz N. 2013. GENSAT BAC Cre-Recombinase Driver Lines to Study the Functional Organization of Cerebral Cortical and Basal Ganglia Circuits. *Neuron* 80: 1368-83

Gouwens NW, Sorensen SA, Berg J, Lee C, Jarsky T, et al. 2019. Classification of electrophysiological and morphological neuron types in the mouse visual cortex. *Nature Neuroscience* 22: 1182-95

Groh A, Meyer HS, Schmidt EF, Heintz N, Sakmann B, Krieger P. 2010. Cell-Type Specific Properties of Pyramidal Neurons in Neocortex Underlying a Layout that Is Modifiable Depending on the Cortical Area. *Cereb Cortex* 20: 826-36

Guerguiev J, Lillicrap TP, Richards BA. 2017. Towards deep learning with segregated dendrites. *eLife* 6

Harnett Mark T, Xu N-L, Magee Jeffrey C, Williams Stephen R. 2013. Potassium Channels Control the Interaction between Active Dendritic Integration Compartments in Layer 5 Cortical Pyramidal Neurons. *Neuron* 79: 516-29

Harris KD, Shepherd GMG. 2015. The neocortical circuit: themes and variations. *Nature Neuroscience* 18: 170-81
Häusser M, Mel B. 2003. Dendrites: bug or feature? *Current Opinion in Neurobiology* 13: 372-83
Hawkins J, Lewis M, Klukas M, Purdy S, Ahmad S. 2019. A Framework for Intelligence and Cortical Function Based on Grid Cells in the Neocortex. *Front. Neural Circuits* 12
Hay E, Hill S, Schürmann F, Markram H, Segev I. 2011. Models of Neocortical Layer 5b Pyramidal Cells Capturing a Wide Range of Dendritic and Perisomatic Active Properties. *PLOS Computational Biology* 7
Jiang X, Shen S, Cadwell CR, Berens P, Sinz F, et al. 2015. Principles of connectivity among morphologically defined cell types in adult neocortex. *Science* 350: aac9462
Kampa BM, Stuart GJ. 2006. Calcium Spikes in Basal Dendrites of Layer 5 Pyramidal Neurons during Action Potential Bursts. *J. Neurosci.* 26: 7424-32
Kasper EM, Larkman AU, Lübke J, Blakemore C. 1994. Pyramidal neurons in layer 5 of the rat visual cortex. I. Correlation among cell morphology, intrinsic electrophysiological properties, and axon targets. *Journal of Comparative Neurology* 339: 459-74
Kim Euiseok J, Juavinett Ashley L, Kyubwa Espoir M, Jacobs Matthew W, Callaway Edward M. 2015. Three Types of Cortical Layer 5 Neurons That Differ in Brain-wide Connectivity and Function. *Neuron* 88: 1253-67
Larkum M. 2013. A cellular mechanism for cortical associations: an organizing principle for the cerebral cortex. *Trends in Neurosciences* 36: 141-51
Larkum ME, Kaiser KMM, Sakmann B. 1999a. Calcium electrogenesis in distal apical dendrites of layer 5 pyramidal cells at a critical frequency of back-propagating action potentials. *PNAS* 96: 14600-04
Larkum ME, Nevian T, Sandler M, Polsky A, Schiller J. 2009. Synaptic Integration in Tuft Dendrites of Layer 5 Pyramidal Neurons: A New Unifying Principle. *Science* 325: 756-60
Larkum ME, Zhu JJ, Sakmann B. 1999b. A new cellular mechanism for coupling inputs arriving at different cortical layers. *Nature* 398: 338-41
London M, Häusser M. 2005. Dendritic Computation. *Annual Review of Neuroscience* 28: 503-32
Lur G, Vinck Martin A, Tang L, Cardin Jessica A, Higley Michael J. 2016. Projection-Specific Visual Feature Encoding by Layer 5 Cortical Subnetworks. *Cell Reports* 14: 2538-45
Mainen ZF, Sejnowski TJ. 1996. Influence of dendritic structure on firing pattern in model neocortical neurons. *Nature* 382: 363-66
Markov NT, Vezoli J, Chameau P, Falchier A, Quilodran R, et al. 2014. Anatomy of hierarchy: Feedforward and feedback pathways in macaque visual cortex. *Journal of Comparative Neurology* 522: 225-59
Markram H, Muller E, Ramaswamy S, Reimann MW, Abdellah M, et al. 2015. Reconstruction and Simulation of Neocortical Microcircuitry. *Cell* 163: 456-92
Miller KD. 2016. Canonical computations of cerebral cortex. *Current Opinion in Neurobiology* 37: 75-84
Mountcastle VB. 1997. The columnar organization of the neocortex. *Brain* 120: 701-22
Noudoost B, Chang MH, Steinmetz NA, Moore T. 2010. Top-down control of visual attention. *Current Opinion in Neurobiology* 20: 183-90
Poirazi P, Brannon T, Mel BW. 2003. Pyramidal Neuron as Two-Layer Neural Network. *Neuron* 37: 989-99
Ramaswamy S, Markram H. 2015. Anatomy and physiology of the thick-tufted layer 5 pyramidal neuron. *Front Cell Neurosci* 9

Rauss K, Schwartz S, Pourtois G. 2011. Top-down effects on early visual processing in humans: A predictive coding framework. *Neuroscience & Biobehavioral Reviews* 35: 1237-53

Rockland KS, Pandya DN. 1979. Laminar origins and terminations of cortical connections of the occipital lobe in the rhesus monkey. *Brain Research* 179: 3-20

Sacramento J, Ponte Costa R, Bengio Y, Senn W. 2018. Dendritic cortical microcircuits approximate the backpropagation algorithm In *Advances in Neural Information Processing Systems 31*, ed. S Bengio, H Wallach, H Larochelle, K Grauman, N Cesa-Bianchi, R Garnett, pp. 8721-32: Curran Associates, Inc.

Schaefer AT, Larkum ME, Sakmann B, Roth A. 2003. Coincidence Detection in Pyramidal Neurons Is Tuned by Their Dendritic Branching Pattern. *Journal of Neurophysiology* 89: 3143-54

Schiller J, Schiller Y, Stuart G, Sakmann B. 1997. Calcium action potentials restricted to distal apical dendrites of rat neocortical pyramidal neurons. *J Physiol* 505: 605-16

Shai AS, Anastassiou CA, Larkum ME, Koch C. 2015. Physiology of Layer 5 Pyramidal Neurons in Mouse Primary Visual Cortex: Coincidence Detection through Bursting. *PLOS Computational Biology* 11

Stuart GJ, Spruston N. 2015. Dendritic integration: 60 years of progress. *Nature Neuroscience* 18: 1713-21

Takahashi N, Oertner TG, Hegemann P, Larkum ME. 2016. Active cortical dendrites modulate perception. *Science* 354: 1587-90

van Ooyen A, Duijnhouwer J, Remme MWH, van Pelt J. 2002. The effect of dendritic topology on firing patterns in model neurons. *Network* 13: 311-25

Vetter P, Roth A, Hausser M. 2001. Propagation of action potentials in dendrites depends on dendritic morphology. *J Neurophysiol* 85: 926-37

Yuste R, Gutnick MJ, Saar D, Delaney KR, Tank DW. 1994. Ca2+ accumulations in dendrites of neocortical pyramidal neurons: An apical band and evidence for two functional compartments. *Neuron* 13: 23-43